INTERNATIONAL JOURNAL FOR NUMERICAL METHODS IN FLUIDS, VOL. 19, 961–979 (1994)

NUMERICAL PREDICTIONS OF THE BIFURCATION OF CONFINED SWIRLING FLOWS

TSUNG LEO JIANG and CHIH-HUNG SHEN

Institute of Aeronautics and Astronautics, National Cheng Kung University, Tainan, Taiwan 70101, R.O.C.

SUMMARY

The bifurcation of confined swirling flows was numerically investigated by employing both the k–ε and algebraic stress turbulence models. Depending upon the branch solution examined, dual flow patterns were predicted at certain swirl levels. In the lower-branch solution which is obtained by gradually increasing the swirl level from a low-swirl flow, the flow changes with increasing swirl number from the low-swirl flow pattern to a high-swirl flow pattern. In the upper-branch solution which is acquired by gradually decreasing the swirl level from a high-swirl flow, on the other hand, the flow can maintain itself in the high-swirl flow pattern at the swirl levels where it exhibits the low-swirl flow pattern in the lower branch. The bifurcation of confined swirling flows was predicted with either the k–ε model or the algebraic stress model being employed. Both the k–ε and algebraic stress models result in comparable and sufficiently good predictions for confined swirling flows if high-order numerical schemes are used. The reported poor performance of the k–ε model was clarified to be mainly attributable to the occurrence of the bifurcation and the use of low-order numerical schemes.

KEY WORDS Confined flow Swirling flow Turbulence model

INTRODUCTION

Swirling flow in a sudden-expansion cylindrical combustor is characterized by two reverse flow zones: the external recirculation zone (ERZ) and the internal recirculation zone (IRZ). The former, resulting from flow separation, is located in the upstream corner region of the combustor. The latter, mainly caused by vortex breakdown of the swirling flow, occurs in the upstream central region of the combustor. When the swirl level is low, the ERZ is longer than the IRZ. This flow pattern is classified as the low-swirl one. As observed in both experimental studies and theoretical predictions,[1] an increase in swirl seems to, at least initially, expand the IRZ in both width and length. This IRZ expansion prevents the ERZ from expanding to the downstream region and the IRZ becomes longer than the ERZ. This flow pattern is thus classified as the high-swirl one. In the transition region between the low- and high-swirl flow patterns, results from the present study suggest that, depending upon the initially assumed flow conditions, dual solutions may be obtained. If the swirl level is gradually decreased from an initially assumed high-swirl flow, the flow can maintain itself in the high-swirl flow pattern at the swirl levels where the low-swirl flow pattern should be exhibited if a low-swirl flow is initially postulated. In other words, both the high- and low-swirl flow patterns may result under equivalent inlet swirl conditions. Apparently, this bifurcation phenomenon is deeply associated with the interference between the two reverse flow zones (ERZ and IRZ).

A similar bifurcation phenomenon, also due to the interference between two reverse flow zones, has been reported in studies of the flow through a plane symmetric sudden expansion,

CCC 0271–2091/94/230961–19

Received January 1994
Revised May 1994

as experimentally documented by Durst *et al.*,[2] Chedron *et al.*,[3] Sobey,[4] Fearn *et al.*[5] and more recently by Durst *et al.*[6] In this case, although the boundary is symmetric, the flow was found to become asymmetric about the central plane as the Reynolds number was increased, resulting in one separation region being larger than the other. The flow could be disturbed from one of the two stable positions to the other by blowing into one separation region through a small tube, as demonstrated by Durst *et al.*[2] The asymmetry remains in the flow even up to turbulent flow conditions,[7] indicating that the bifurcation of the flow through a plane symmetric sudden expansion may occur in both laminar and turbulent flows. Asymmetric steady flows are exhibited, however, only when the Reynolds number exceeds a critical value or the interference between both reverse flow zones is sufficiently strong, a situation similar to the bifurcation of a confined swirling flow.

Although the bifurcation of a confined swirling flow has not been reported previously, its occurrence has in fact been implicitly exhibited in certain published works. For instance, when Sloan *et al.*[1] evaluated various turbulence models for swirling flows by comparing predictions with the experimental data of Yoon and Lilley,[8,9] the low- and high-swirl flow patterns were predicted by the k–ε model for the 38° and 45° swirl vane angle cases respectively. Since the measurements exhibited the high-swirl flow pattern for both swirl vane angle cases, the discrepant predictions were thus attributed to the poor performance of the k–ε mode.[1] However, since the difference in the swirl vane angle is small (only 7°), it is unusual for the k–ε model to give very different flow predictions for the two cases. As illustrated later in the present study, these two flow predictions are in fact coincident with the low- and high-swirl flow patterns respectively. For the 38° swirl vane angle case the high-swirl flow pattern can also be predicted by the k–ε model as long as the solution is obtained by gradually decreasing the swirl level from an initially assumed high-swirl flow. In other words, the poor performance of the k–ε model reported by Sloan *et al.*[1] for the prediction of Yoon and Lilley's experiments[8,9] may be mainly attributed to the occurrence of the bifurcation rather than the model's incapability. The second piece of evidence for the bifurcation of a confined swirling flow is found in a work presented by Weber *et al.*[10] in assessing turbulence modelling for the engineering prediction of swirling vortices in the near-burner zone. Weber *et al.* concluded that reliable predictions can be made if fine numerical grids are used in conjunction with the QUICK method (a high-order numerical scheme) as well as the algebraic stress model (ASM). The k–ε model was reported to perform poorly in the prediction of confined swirling flows. An examination of the flow patterns presented by Weber *et al.*,[10] however, reveals that the flow patterns predicted by the k–ε model and the ASM are coincident with the low- and high-swirl flow patterns respectively. It is thus suspected that the discrepant predictions of the flow patterns may also be due to the occurrence of the bifurcation rather than the poor performance of the k–ε model, since by using the k–ε model in conjunction with high-order convection–diffusion schemes, satisfactory predictions of a confined double-concentric swirling flow have been reported recently by Durst and Wennerberg.[11]

The occurrence of the bifurcation may thus be deeply involved with regard to the engineering prediction of a confined swirling flow. However, it has never been discovered previously. In the present study this bifurcation phenomenon is explored through a numerical analysis with either the k–ε model or the ASM being employed. Effects of both the low- and high-order numerical schemes on the prediction of a confined swirling flow are also investigated, especially for situations where the bifurcation occurs. Therefore the influences of the bifurcation phenomenon, turbulence models and numerical schemes on the prediction of a confined swirling flow can be clarified. In particular, the cause for the poor performance of the k–ε model reported by Sloan *et al.*[1] is identified and the relative importance of numerical schemes with respect to turbulence models in obtaining satisfactory predictions for this particular case is also examined.

FORMULATIONS

The test section of the experiments conducted by Yoon and Lilley[8,9] serves as the basis of the present study (see Figure 1(a)). The single air stream enters the test section through a secondary annulus, passing through an adjustable vane swirler. The continuity and momentum equations governing such an axisymmetric swirling flow can be expressed as

$$\frac{\partial}{\partial x}(\rho\bar{u}) + \frac{1}{r}\frac{\partial}{\partial r}(r\rho\bar{v}) = 0, \tag{1}$$

$$\frac{\partial}{\partial x}\left(\rho\bar{u}\bar{u} - \mu\frac{\partial\bar{u}}{\partial x}\right) + \frac{1}{r}\frac{\partial}{\partial r}\left(r\rho\bar{v}\bar{u} - r\mu\frac{\partial\bar{u}}{\partial r}\right) = -\frac{\partial\bar{p}}{\partial x} + \frac{\partial}{\partial x}\left(\mu\frac{\partial\bar{u}}{\partial x}\right) + \frac{1}{r}\frac{\partial}{\partial r}\left(r\mu\frac{\partial\bar{v}}{\partial x}\right) - \frac{\partial}{\partial x}(\rho\overline{u'u'}) - \frac{1}{r}\frac{\partial}{\partial r}(r\rho\overline{u'v'}), \tag{2}$$

$$\frac{\partial}{\partial x}\left(\rho\bar{u}\bar{v} - \mu\frac{\partial\bar{v}}{\partial x}\right) + \frac{1}{r}\frac{\partial}{\partial r}\left(r\rho\bar{v}\bar{v} - r\mu\frac{\partial\bar{v}}{\partial r}\right) = -\frac{\partial\bar{p}}{\partial r} + \frac{\partial}{\partial x}\left(\mu\frac{\partial\bar{u}}{\partial r}\right) + \frac{1}{r}\frac{\partial}{\partial r}\left(r\mu\frac{\partial\bar{v}}{\partial r}\right) - \frac{2}{r^2}\mu\bar{v} + \frac{\rho}{r}(\bar{w}^2 + \overline{w'w'}) - \frac{\partial}{\partial x}(\rho\overline{u'v'}) - \frac{1}{r}\frac{\partial}{\partial r}(r\rho\overline{v'v'}), \tag{3}$$

$$\frac{\partial}{\partial x}\left(\rho\bar{u}\bar{w} - \mu\frac{\partial\bar{w}}{\partial x}\right) + \frac{1}{r}\frac{\partial}{\partial r}\left(r\rho\bar{v}\bar{w} - r\mu\frac{\partial\bar{w}}{\partial r}\right) = -\frac{1}{r}(\rho\bar{v}\bar{w} + \rho\overline{v'w'}) - \frac{\bar{w}}{r^2}\frac{\partial}{\partial r}(r\mu) - \frac{\partial}{\partial x}(\rho\overline{u'w'}) - \frac{1}{r}\frac{\partial}{\partial r}(r\rho\overline{v'w'}). \tag{4}$$

Owing to the classical closure problem in turbulence theory, the Reynolds stresses must be related to known or calculable mean flow field variables. Two turbulence models were considered in this study, the k–ε model and the ASM, which are elaborated in the following.

The k–ε model

The k–ε model assumes that the Reynolds stress is proportional to the mean velocity gradient. The constant of proportionality, denoted the eddy or turbulence viscosity, is given by

$$\mu^t = C_\mu\rho\frac{k^2}{\varepsilon}, \tag{5}$$

where the turbulent kinetic energy k and the turbulent dissipation rate ε satisfy the respective transport equations

$$\frac{\partial}{\partial x}\left(\rho\bar{u}k - \frac{\mu^e}{\sigma_k}\frac{\partial k}{\partial x}\right) + \frac{1}{r}\frac{\partial}{\partial r}\left(r\rho\bar{v}k - r\frac{\mu^e}{\sigma_k}\frac{\partial k}{\partial r}\right) = g - \rho\varepsilon, \tag{6}$$

$$\frac{\partial}{\partial x}\left(\rho\bar{u}\varepsilon - \frac{\mu^e}{\sigma_\varepsilon}\frac{\partial\varepsilon}{\partial x}\right) + \frac{1}{r}\frac{\partial}{\partial r}\left(r\rho\bar{v}\varepsilon - r\frac{\mu^e}{\sigma_\varepsilon}\frac{\partial\varepsilon}{\partial r}\right) = C_{\varepsilon1}g\frac{\varepsilon}{k} - C_{\varepsilon2}\rho\frac{\varepsilon^2}{k}, \tag{7}$$

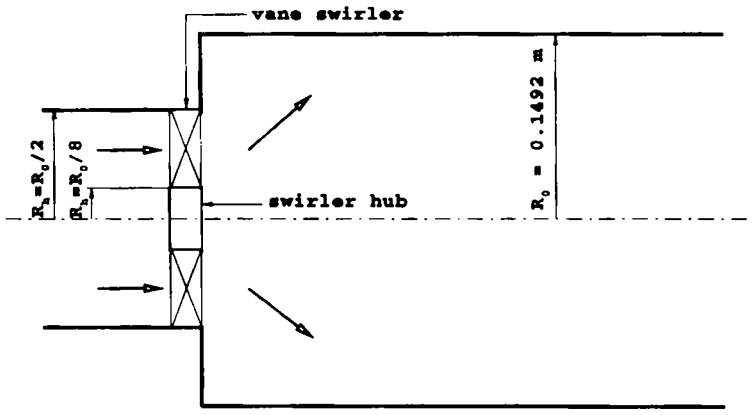

(a)

(b)

Figure 1. (a) Schematic diagram of Yoon and Lilley[8] test section. (b) Grid system employed for computations (42 × 32)

with

$$g = \mu^t\left\{2\left[\left(\frac{\partial \bar{u}}{\partial x}\right)^2 + \left(\frac{\partial \bar{v}}{\partial r}\right)^2 + \left(\frac{\bar{v}}{r}\right)^2\right] + \left[r\frac{\partial}{\partial r}\left(\frac{\bar{w}}{r}\right)\right]^2 + \left(\frac{\partial \bar{v}}{\partial x} + \frac{\partial \bar{u}}{\partial r}\right)^2 + \left(\frac{\partial \bar{w}}{\partial x}\right)^2\right\}. \tag{8}$$

Here μ^e denotes the effective viscosity, defined as $\mu^e = \mu + \mu^t$. The resultant momentum equations of the k–ε model are thus given as

$$\frac{\partial}{\partial x}\left(\rho\bar{u}\bar{u} - \mu^e\frac{\partial \bar{u}}{\partial x}\right) + \frac{1}{r}\frac{\partial}{\partial r}\left(r\rho\bar{v}\bar{u} - r\mu^e\frac{\partial \bar{u}}{\partial r}\right) = -\frac{\partial}{\partial x}(\bar{p} + \tfrac{2}{3}\rho k) + \frac{\partial}{\partial x}\left(\mu^e\frac{\partial \bar{u}}{\partial x}\right) + \frac{1}{r}\frac{\partial}{\partial r}\left(r\mu^e\frac{\partial \bar{v}}{\partial x}\right), \tag{9}$$

$$\frac{\partial}{\partial x}\left(\rho\bar{u}\bar{v} - \mu^e\frac{\partial \bar{v}}{\partial x}\right) + \frac{1}{r}\frac{\partial}{\partial r}\left(r\rho\bar{v}\bar{v} - r\mu^e\frac{\partial \bar{v}}{\partial r}\right)$$
$$= -\frac{\partial}{\partial r}(\bar{p} + \tfrac{2}{3}\rho k) + \frac{\partial}{\partial x}\left(\mu^e\frac{\partial \bar{u}}{\partial r}\right) + \frac{1}{r}\frac{\partial}{\partial r}\left(r\mu^e\frac{\partial \bar{v}}{\partial r}\right) - \frac{2}{r^2}\mu^e\bar{v} + \frac{\rho}{r}\bar{w}^2, \tag{10}$$

$$\frac{\partial}{\partial x}\left(\rho\bar{u}\bar{w}-\mu^{e}\frac{\partial\bar{w}}{\partial x}\right)+\frac{1}{r}\frac{\partial}{\partial r}\left(r\rho\bar{v}\bar{w}-r\mu^{e}\frac{\partial\bar{w}}{\partial r}\right)=-\frac{1}{r}(\rho\bar{v}\bar{w})-\frac{\bar{w}}{r^{2}}\frac{\partial}{\partial r}(r\mu^{e}). \tag{11}$$

The algebraic stress model (ASM)

Adopting Rodi's approximation that the local value of $\overline{u_i'u_j'}/k$ is spatially invariant, the Reynolds stress transport equations may be reduced to their algebraic equivalent[1] and the resultant algebraic equations for the six Reynolds stresses are given as

$$\begin{bmatrix}
\alpha+2\frac{\partial\bar{u}}{\partial x} & -\frac{\partial\bar{v}}{\partial r} & -\frac{\bar{v}}{r} & -\left(\frac{\partial\bar{v}}{\partial x}-2\frac{\partial\bar{u}}{\partial r}\right) & -\frac{\partial\bar{w}}{\partial x} & -\left(\frac{\partial\bar{w}}{\partial r}-\frac{\bar{w}}{r}\right)\\
-\frac{\partial\bar{u}}{\partial x} & \alpha+2\frac{\partial\bar{v}}{\partial r} & -\frac{\bar{v}}{r} & -\left(\frac{\partial\bar{u}}{\partial r}-2\frac{\partial\bar{v}}{\partial x}\right) & -\frac{\partial\bar{w}}{\partial x} & -\left(\frac{\partial\bar{w}}{\partial r}+2\frac{\bar{w}}{r}\right)\\
-\frac{\partial\bar{u}}{\partial x} & -\frac{\partial\bar{v}}{\partial r} & \alpha+2\frac{\bar{v}}{r} & -\left(\frac{\partial\bar{u}}{\partial r}+\frac{\partial\bar{v}}{\partial x}\right) & 2\frac{\partial\bar{w}}{\partial x} & 2\frac{\partial\bar{w}}{\partial r}+\frac{\bar{w}}{r}\\
\frac{\partial\bar{v}}{\partial x} & \frac{\partial\bar{u}}{\partial r} & 0 & \beta-\frac{\bar{v}}{r} & -\frac{\bar{w}}{r} & 0\\
\frac{\partial\bar{w}}{\partial x} & 0 & 0 & \frac{\partial\bar{w}}{\partial r} & \beta-\frac{\partial\bar{v}}{\partial r} & \frac{\partial\bar{u}}{\partial r}\\
0 & \frac{\partial\bar{w}}{\partial r} & -\frac{\bar{w}}{r} & \frac{\partial\bar{w}}{\partial x} & \frac{\partial\bar{v}}{\partial x} & \beta-\frac{\partial\bar{u}}{\partial x}
\end{bmatrix}\begin{bmatrix}\rho\overline{u'u'}\\ \rho\overline{v'v'}\\ \rho\overline{w'w'}\\ \rho\overline{u'v'}\\ \rho\overline{u'w'}\\ \rho\overline{v'w'}\end{bmatrix}=\begin{bmatrix}\rho\gamma\\ \rho\gamma\\ \rho\gamma\\ 0\\ 0\\ 0\end{bmatrix}, \tag{12}$$

where

$$\lambda=\frac{1-C_{\mathrm{ASM},2}}{C_{\mathrm{ASM},1}-1+P/\varepsilon},\qquad \gamma=\frac{\varepsilon}{\lambda},\qquad \beta=\frac{\gamma}{k},\qquad \alpha=\tfrac{3}{2}\beta.$$

For the convenience of numerical computation, the governing equations are usually required to be composed of distinct convective, diffusive and source terms. In the ASM, however, the diffusion terms of the governing equations only involve the laminar diffusion and are substantially smaller than the convective terms, causing a problem of numerical stability. Therefore equivalent eddy viscosity diffusion terms are added and subtracted in the governing equations in order to overcome this problem.[10] As a result, the k- and ε-equations in the ASM are given as

$$\begin{aligned}
&\frac{\partial}{\partial x}\left(\rho\bar{u}k-\frac{\mu^{e}}{\sigma_k}\frac{\partial k}{\partial x}\right)+\frac{1}{r}\frac{\partial}{\partial r}\left(r\rho\bar{v}k-r\frac{\mu^{e}}{\sigma_k}\frac{\partial k}{\partial r}\right)\\
&\quad=g-\rho\varepsilon+\frac{\partial}{\partial x}\left\{\left[\rho C_k\left(\frac{k}{\varepsilon}\right)\overline{u'u'}-\frac{\mu^{t}}{\sigma_k}\right]\frac{\partial k}{\partial x}+\rho C_k\left(\frac{k}{\varepsilon}\right)\overline{u'v'}\frac{\partial k}{\partial r}\right\}\\
&\qquad+\frac{1}{r}\frac{\partial}{\partial r}\left\{r\left[\rho C_k\left(\frac{k}{\varepsilon}\right)\overline{v'v'}-\frac{\mu^{t}}{\sigma_k}\right]\frac{\partial k}{\partial r}+r\rho C_k\left(\frac{k}{\varepsilon}\right)\overline{u'v'}\frac{\partial k}{\partial x}\right\},
\end{aligned} \tag{13}$$

$$\frac{\partial}{\partial x}\left(\rho\bar{u}\varepsilon - \frac{\mu^e}{\sigma_\varepsilon}\frac{\partial\varepsilon}{\partial x}\right) + \frac{1}{r}\frac{\partial}{\partial r}\left(r\rho\bar{v}\varepsilon - r\frac{\mu^e}{\sigma_\varepsilon}\frac{\partial\varepsilon}{\partial r}\right)$$
$$= C_{\varepsilon 1} g \frac{\varepsilon}{k} - C_{\varepsilon 2}\rho\frac{\varepsilon^2}{k} + \frac{\partial}{\partial x}\left\{\left[\rho C_{\varepsilon 3}\left(\frac{k}{\varepsilon}\right)\overline{u'u'} - \frac{\mu^t}{\sigma_\varepsilon}\right]\frac{\partial\varepsilon}{\partial x} + \rho C_{\varepsilon 3}\left(\frac{k}{\varepsilon}\right)\overline{u'v'}\frac{\partial\varepsilon}{\partial r}\right\}$$
$$+ \frac{1}{r}\frac{\partial}{\partial r}\left\{r\left[\rho C_{\varepsilon 3}\left(\frac{k}{\varepsilon}\right)\overline{v'v'} - \frac{\mu^t}{\sigma_\varepsilon}\right]\frac{\partial\varepsilon}{\partial r} + r\rho C_{\varepsilon 3}\left(\frac{k}{\varepsilon}\right)\overline{u'v'}\frac{\partial\varepsilon}{\partial x}\right\}, \tag{14}$$

where

$$g = -\rho\left[\overline{u'u'}\left(\frac{\partial\bar{u}}{\partial x}\right) + \overline{v'v'}\left(\frac{\partial\bar{v}}{\partial r}\right) + \overline{w'w'}\left(\frac{\bar{v}}{r}\right) + \overline{u'v'}\left(\frac{\partial\bar{v}}{\partial x} + \frac{\partial\bar{u}}{\partial r}\right) + \overline{u'w'}\left(\frac{\partial\bar{w}}{\partial x}\right) + \overline{v'w'}\left(\frac{\partial\bar{w}}{\partial r} - \frac{\bar{w}}{r}\right)\right]. \tag{15}$$

The momentum equations associated with the ASM are expressed as

$$\frac{\partial}{\partial x}\left(\rho\bar{u}\bar{u} - \mu^e\frac{\partial\bar{u}}{\partial x}\right) + \frac{1}{r}\frac{\partial}{\partial r}\left(r\rho\bar{v}\bar{u} - r\mu^e\frac{\partial\bar{u}}{\partial r}\right) = -\frac{\partial\bar{p}}{\partial x} + \frac{\partial}{\partial x}\left(\mu\frac{\partial\bar{u}}{\partial x}\right) + \frac{1}{r}\frac{\partial}{\partial r}\left(r\mu\frac{\partial\bar{v}}{\partial x}\right) - \frac{\partial}{\partial x}(\rho\overline{u'u'})$$
$$- \frac{1}{r}\frac{\partial}{\partial r}(r\rho\overline{u'v'}) - \frac{\partial}{\partial x}\left(\mu^t\frac{\partial\bar{u}}{\partial x}\right) - \frac{1}{r}\frac{\partial}{\partial r}\left(r\mu^t\frac{\partial\bar{u}}{\partial r}\right), \tag{16}$$

$$\frac{\partial}{\partial x}\left(\rho\bar{u}\bar{v} - \mu^e\frac{\partial\bar{v}}{\partial x}\right) + \frac{1}{r}\frac{\partial}{\partial r}\left(r\rho\bar{v}\bar{v} - r\mu^e\frac{\partial\bar{v}}{\partial r}\right)$$
$$= -\frac{\partial\bar{p}}{\partial r} + \frac{\partial}{\partial x}\left(\mu\frac{\partial\bar{u}}{\partial r}\right) + \frac{1}{r}\frac{\partial}{\partial r}\left(r\mu\frac{\partial\bar{v}}{\partial r}\right) - \frac{2}{r^2}\mu\bar{v} + \frac{\rho}{r}(\bar{w}^2 + \overline{w'w'})$$
$$- \frac{\partial}{\partial x}(\rho\overline{u'v'}) - \frac{1}{r}\frac{\partial}{\partial r}(r\rho\overline{v'v'}) - \frac{\partial}{\partial x}\left(\mu^t\frac{\partial\bar{v}}{\partial x}\right) - \frac{1}{r}\frac{\partial}{\partial r}\left(r\mu^t\frac{\partial\bar{v}}{\partial r}\right), \tag{17}$$

$$\frac{\partial}{\partial x}\left(\rho\bar{u}\bar{w} - \mu^e\frac{\partial\bar{w}}{\partial x}\right) + \frac{1}{r}\frac{\partial}{\partial r}\left(r\rho\bar{v}\bar{w} - r\mu^e\frac{\partial\bar{w}}{\partial r}\right)$$
$$= -\frac{1}{r}(\rho\bar{v}\bar{w} + \rho\overline{v'w'}) - \frac{\bar{w}}{r^2}\frac{\partial}{\partial r}(r\mu) - \frac{\partial}{\partial x}(\rho\overline{u'w'}) - \frac{1}{r}\frac{\partial}{\partial r}(r\rho\overline{v'w'}) - \frac{\partial}{\partial x}\left(\mu^t\frac{\partial\bar{w}}{\partial x}\right) - \frac{1}{r}\frac{\partial}{\partial r}\left(r\mu^t\frac{\partial\bar{w}}{\partial r}\right). \tag{18}$$

The turbulence model constants adopted in the present study are $C_\mu = 0{\cdot}09$, $\sigma_k = 0{\cdot}9$, $\sigma_\varepsilon = 1{\cdot}22$, $C_k = 0{\cdot}22$, $C_{\varepsilon 1} = 1{\cdot}44$, $C_{\varepsilon 2} = 1{\cdot}92$, $C_{\varepsilon 3} = 0{\cdot}15$, $C_{\text{ASM},1} = 2{\cdot}5$ and $C_{\text{ASM},2} = 0{\cdot}55$.

Inlet and boundry conditions

The inlet k was assumed as $k_{\text{in}} = R_k\bar{u}_{\text{in}}^2$, where $R_k = 0{\cdot}039$, and for the inlet ε the equation proposed by Sturgess *et al.*[12] was adopted, i.e. $\varepsilon_{\text{in}} = k_{\text{in}}^{1{\cdot}5}/0{\cdot}333l$, where l is a characteristic dimension of the flow passage and is assumed to be one-tenth of the difference between the outer and inner diameters of a vane swirler that has 10 vanes.[8] In order to identify the cause of the unusual predictions of Sloan *et al.*,[1] the same inlet axial and radial velocity profiles as those of Sloan *et al.*'s computations[1] for the 38° swirl vane angle case of Yoon and Lilley's experiments[8,9] are assumed. The inlet tangential velocity profile is, however, assumed proportional to that of the 38° swirl vane angle case. Thus different swirl numbers, defined as $SN = \int_0^{R_i} r^2\rho uw\,\mathrm{d}r/(R_i\int_0^{R_i} r\rho uu\,\mathrm{d}r)$, are obtained simply by changing the proportionality constant

for the inlet tangential velocity. For the 38° swirl vane angle case the assumed inlet velocity profiles are thus exactly the same as the inlet data assumed by Sloan *et al.*[1] It is noted that as the vane angle changes, not only the inlet tangential but also the inlet axial and radial velocities vary. Therefore the inlet axial and radial velocity profiles assumed in this manner are simply for convenience to identify the bifurcation phenomenon. The wall function method[1,13] is adopted for both the k–ε model and the ASM in order to eliminate the need for fine grids in the near-wall region of a turbulent flow. A zero-gradient condition for all variables and a zero radial velocity are applied at the symmetry axis. At the outlet stream the axial velocity is determined from the overall mass conservation, while the radial velocity is set to zero. The other variables are assumed to follow the local one-way behaviour[14] and need no specific information at the outlet boundary.

Solution procedure

The governing equations are discretized into their algebraic counterparts based on the finite volume method, and the SIMPLER algorithm[14] is applied to solve the gas flow field. The line-by-line tridiagonal matrix algorithm (TDMA), featuring a back-and-forth sweep that alternates in direction, is used as the equation solver and incorporates the block correction procedure[15] for increased computational efficiency. The power law scheme[14] is used for the convective and diffusive fluxes over the control volume surface. For the flow computation with a high-order numerical scheme, the second-order upwind (SOU) scheme[16] is employed for the velocity calculations. A staggered grid system is adopted to avoid zigzag pressure and velocity distributions. Thus all scalar quantities are stored at the nodal points of cells, whereas velocity components are stored on the cell faces. An orthogonal non-uniform grid system consisting of 42 × 32 grids (see Figure 1(b)) is employed, with grids being contracted towards the solid walls. Grid independence has been achieved, since a 50% increase in axial or radial grids results in no significant discrepancies in predictions. Rigorous convergence is assured by requiring the maximum residual of the numerical equations to reduce to a prescribed small value and the relative difference in the variables between two iterations to be smaller than 10^{-4}. As a result, more than 5000 iterations are needed for some computations employing the ASM.

RESULTS AND DISCUSSION

For the flow configuration depicted in Figure 1(a) both an ERZ and an IRZ result. The ERZ is due to the flow separation occurring around the chamber corner, while the IRZ is caused not only by the vortex breakdown of the swirling flow but also by the existence of the swirler hub acting as a solid wall. Therefore even at the no-swirl limit the IRZ is still expected to exist because of the latter situation.

The bifurcation phenomenon

In Figure 2 the ratio of the maximum reverse flow rate of the IRZ to that of the ERZ versus the swirl number is presented for both the lower- and upper-branch solutions. These results were yielded by using the k–ε model in conjunction with the power law scheme, similarly to those adopted by Sloan *et al.*[1] The lower-branch solution was obtained by gradually increasing the swirl level from a low-swirl flow, while the upper-branch solution was acquired by gradually decreasing the swirl level from a high-swirl flow. It is interesting to note that a hysteresis effect results as the swirl number increases from 0·34 up to 0·46 along the lower branch and then decreases back to 0·34 following the upper branch, resulting in dual solutions in the swirl number

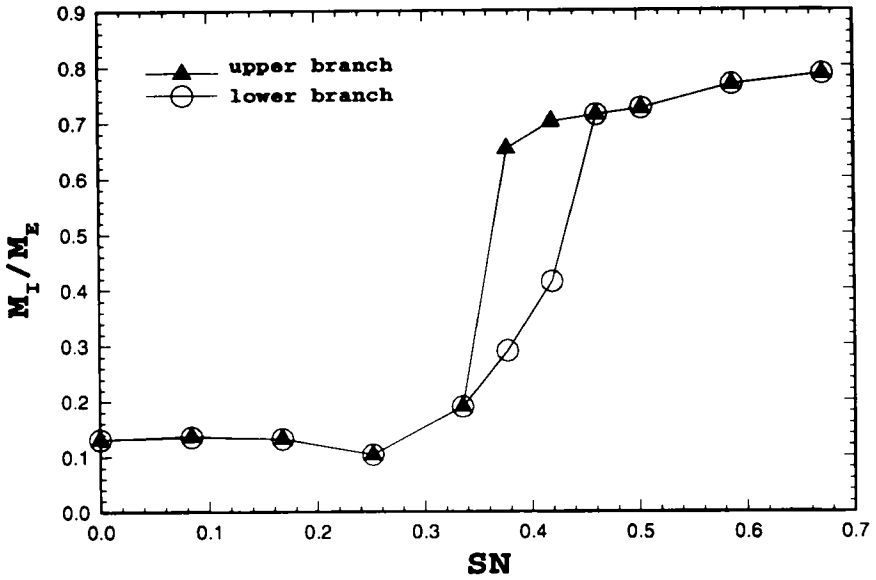

Figure 2. Ratio of the maximum reverse flow rate of the IRZ to that of the ERZ versus the swirl number predicted by both the lower and upper branches using the k–ε model in conjunction with the power law scheme

range from 0·34 to 0·46. An examination of the flow patterns within this small swirl number range (see Figure 3(a)–3(d) and 4(a)–4(d)) reveals that two different flow patterns can be identified associated with this hysteresis effect. One is characterized by a prolonged ERZ and a laterally flat IRZ, classified here as the low-swirl flow pattern, and the other is characterized by a limited size ERZ and a laterally expanding IRZ, classified here as the high-swirl flow pattern. In the lower-branch solution (Figures 3(a)–3(d)) the low-swirl flow pattern is exhibited when the swirl number is smaller than 0·46 (Figures 3(a)–3(c)), since the swirl is not sufficiently strong to prevent the ERZ from expanding towards the downstream region. The low-swirl flow pattern changes to the high-swirl one only when the swirl number is sufficiently large, such as 0·46 for the present case (Figure 3(d)). With such a relatively large swirl number the IRZ expands laterally and prevents the adjacent ERZ from expanding forwards. In the upper-branch solution, on the other hand, the high-swirl flow pattern is exhibited when the swirl number is larger than 0·34 (Figures 4(b)–4(d)). The IRZ is maintained relatively stronger at the swirl numbers where it is relatively weaker in the lower branch (compare Figures 3(b), 3(c) and 4(b), 4(c)). The high-swirl flow pattern does not change to the low-swirl one until the swirl number is sufficiently low, such as 0·34 for the present case (Figure 4(a)). As a result, depending upon the branch solution examined, the flow exhibits dual patterns at a swirl number between the two values of 0·34 and 0·46. For the swirl number either smaller than 0·34 or greater than 0·46, however, the low- and high-swirl flow patterns are exhibited for the former and the latter respectively. In these cases only a single flow pattern is predicted and both branch solutions are identical. An examination of the variations in flow patterns with the swirl number in the lower and upper branches reveals that the occurrence of the bifurcation of a confined swirling flow stems from a hysteresis effect as the high-swirl flow pattern changes to the low-swirl one with the gradually decreasing swirl level. The hysteresis effect is yielded, however, mainly owing to a relatively stronger IRZ, which

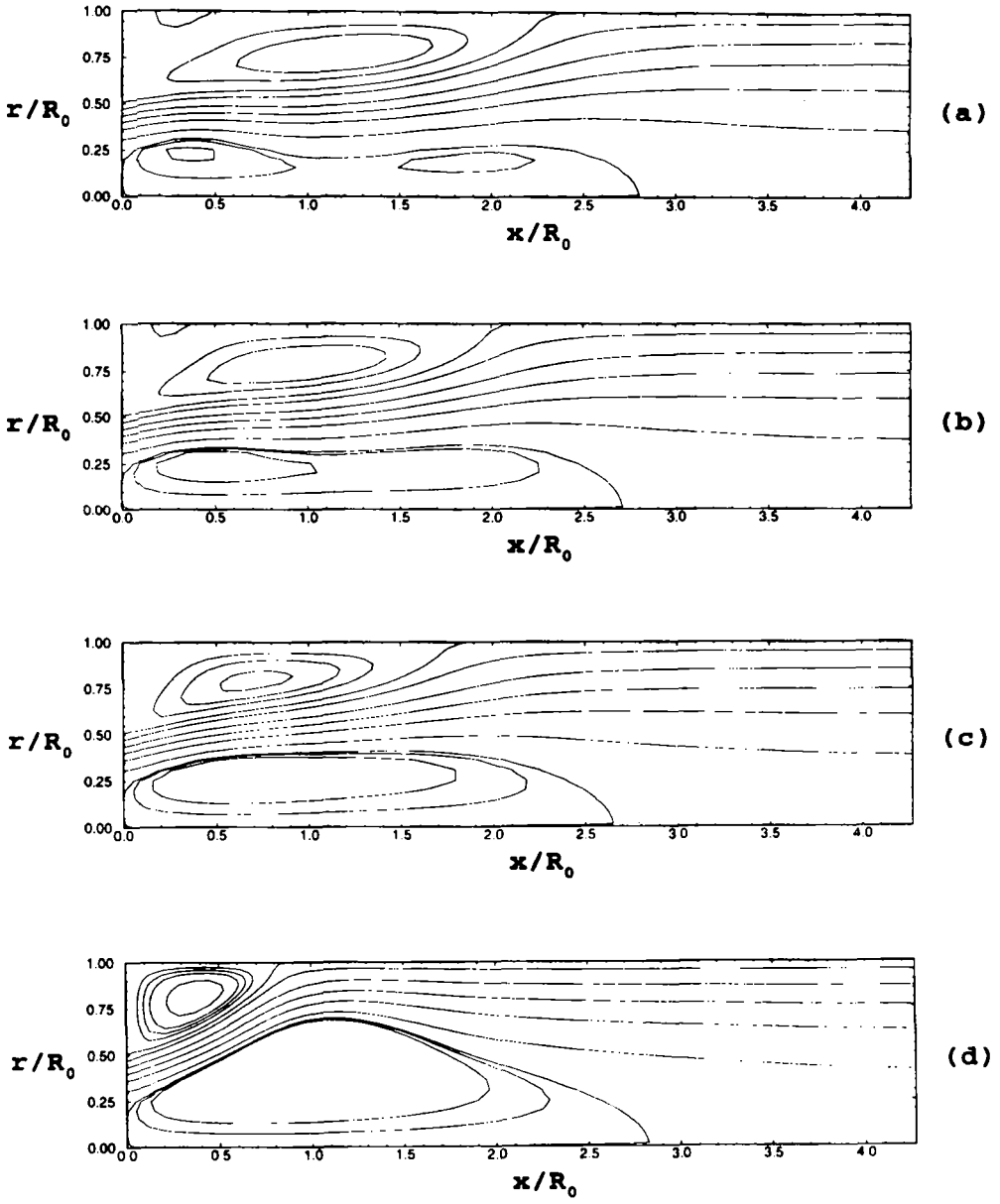

Figure 3. Flow patterns predicted by the lower branch for swirl numbers of (a) 0·34, (b) 0·38, (c) 0·42 and (d) 0·46 using the k–ε model in conjunction with the power law scheme

prevents the expansion of the ERZ. In other words, whether the IRZ is sufficiently strong with respect to the ERZ determines the occurrence of the bifurcation.

The bifurcation of these swirling flow cases offers an explanation of the unusual predictions of Sloan *et al.*,[1] since the swirl number of the 38° swirl vane angle case (SN = 0·42) is just within this bifurcation solution range. As depicted in Figure 5, where the axial velocity profiles at two axial positions, x/R_0 = 1·0 and 2·0, predicted by both the lower- and upper-branch solutions are

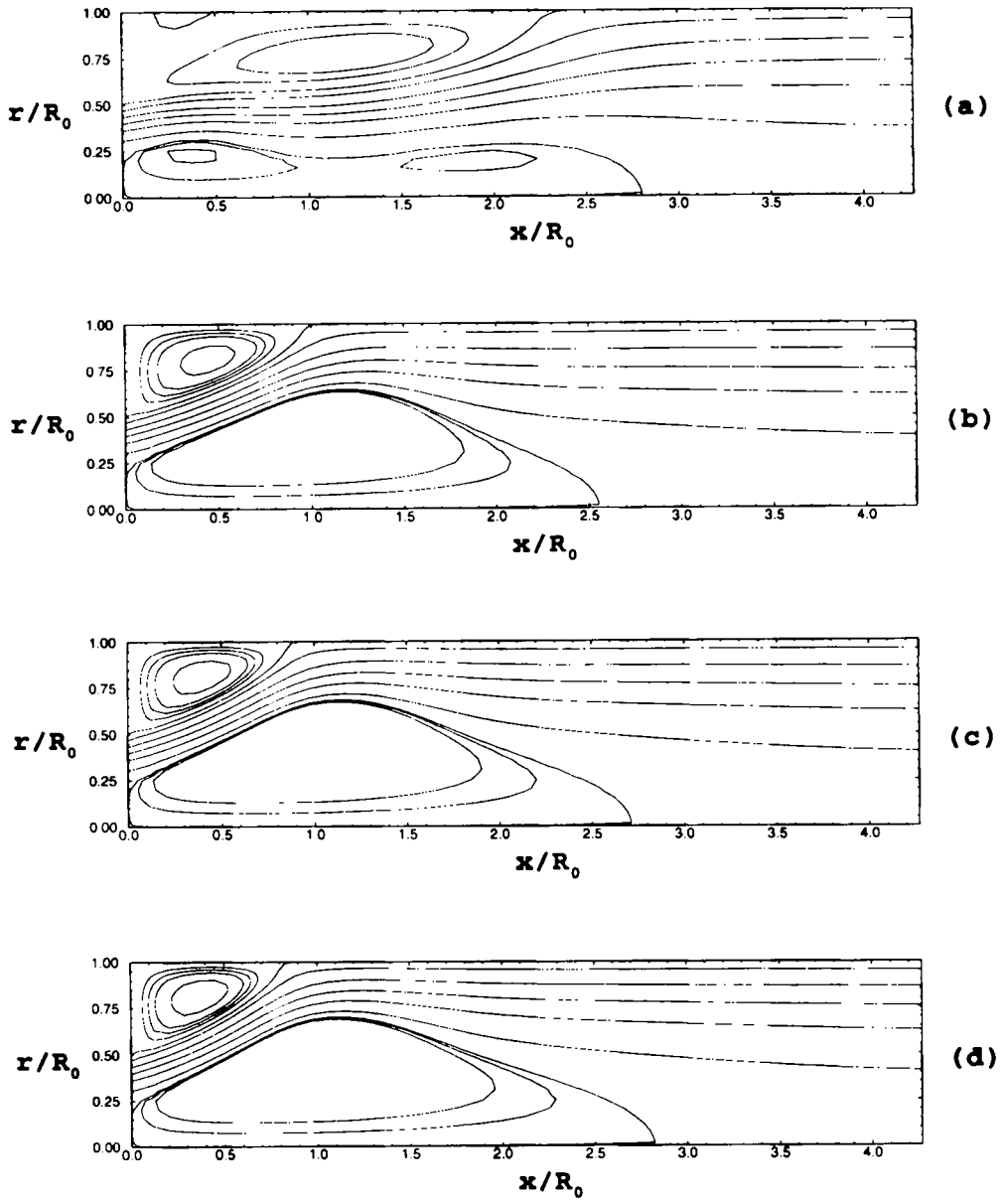

Figure 4. Flow patterns predicted by the upper branch for swirl numbers of (a) 0·34, (b) 0·38, (c) 0·42 and (d) 0·46 using the k–ε model in conjunction with the power law scheme

presented in comparison with the experimental data of Yoon and Lilley,[8,9] the lower-branch solution, similarly to the predictions of Sloan *et al.*,[1] deviates significantly from the experimental result. The upper branch solution, however, yields a result in better agreement with the experimental data. The poor performance of the k–ε model for the 38° swirl vane angle case reported by Sloan *et al.*[1] is thus clarified to be mainly attributable to the occurrence of the bifurcation flow solutions. If the upper-branch solution is selected, the k–ε model in fact produces a result comparable with that of other turbulence models.

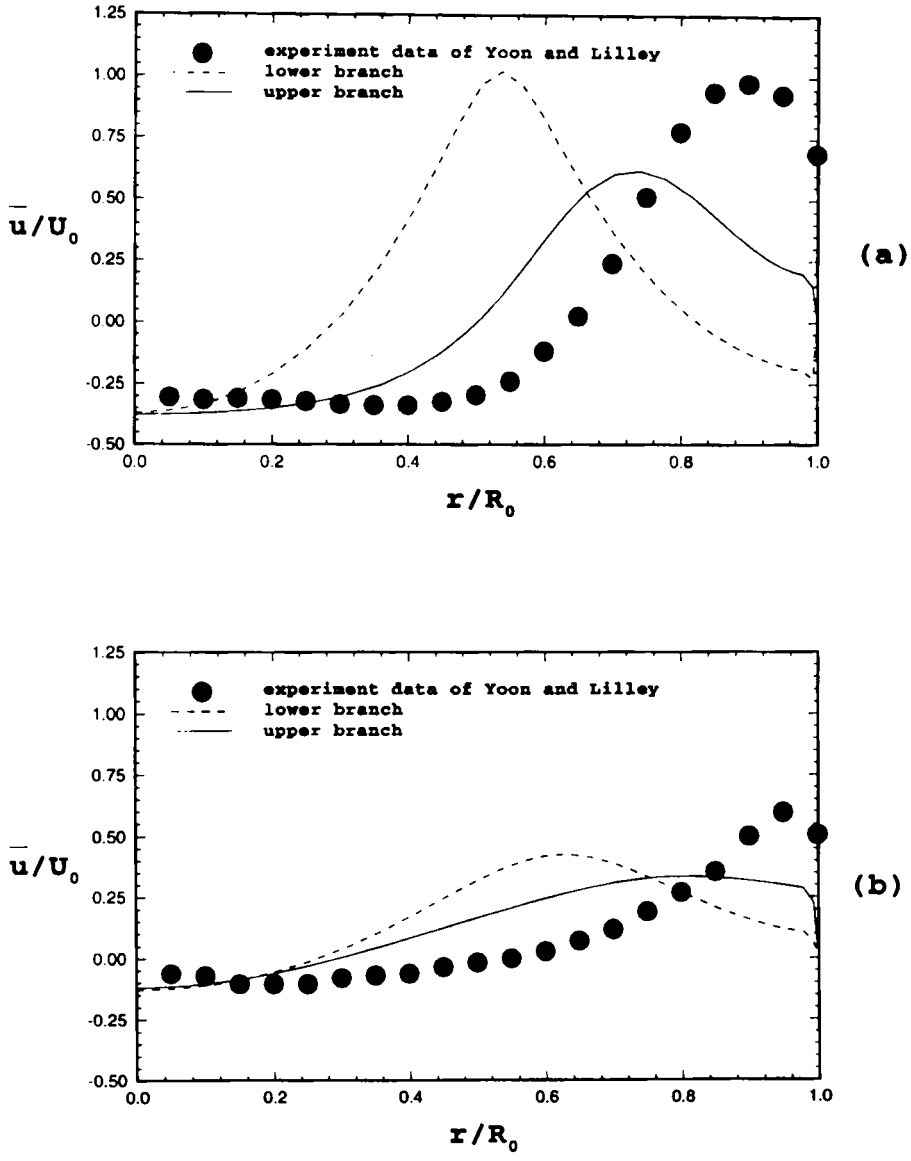

Figure 5. Axial velocity profiles for the 38° swirl vane angle case predicted by both the lower and upper branches using the k–ε model in conjunction with the power law scheme at x/R_0 = (a) 1·0 and (b) 2·0

Effects of numerical schemes

For a confined swirling flow the appearance of the IRZ causes the flow direction to be inclined relative to the grid orientation of the normally employed orthogonal grid system, resulting in significant numerical diffusion. As demonstrated by Weber *et al.*[10] and Durst and Wennerberg[11] for such a flow configuration, high-order convection–diffusion schemes can diminish the numerical diffusion and produce very different results from those by low-order schemes. Therefore the bifurcation phenomenon is also affected by the use of different numerical schemes. As depicted in Figure 6, the predicted ratio of the maximum reverse flow rate of the

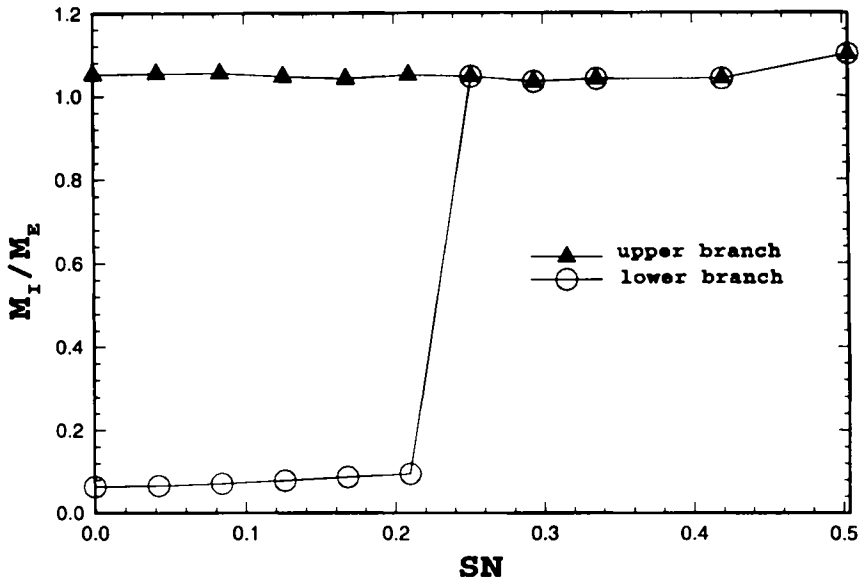

Figure 6. Ratio of the maximum reverse flow rate of the IRZ to that of the ERZ versus the swirl number predicted by both the lower and upper branches using the k–ε model in conjunction with the second-order upwind scheme

IRZ to that of the ERZ versus the swirl number also exhibits dual solutions for a certain swirl number range by using the k–ε model in conjunction with the second-order upwind scheme. The bifurcation solutions are predicted to occur at swirl numbers smaller than 0·25. An examination of the predicted bifurcation flow patterns (see Figures 7(a), 7(b) and 8(a), 8(b)) reveals that dual flow patterns are exhibited at a swirl number of 0·21 (Figures 7(a) and 7(b) with the

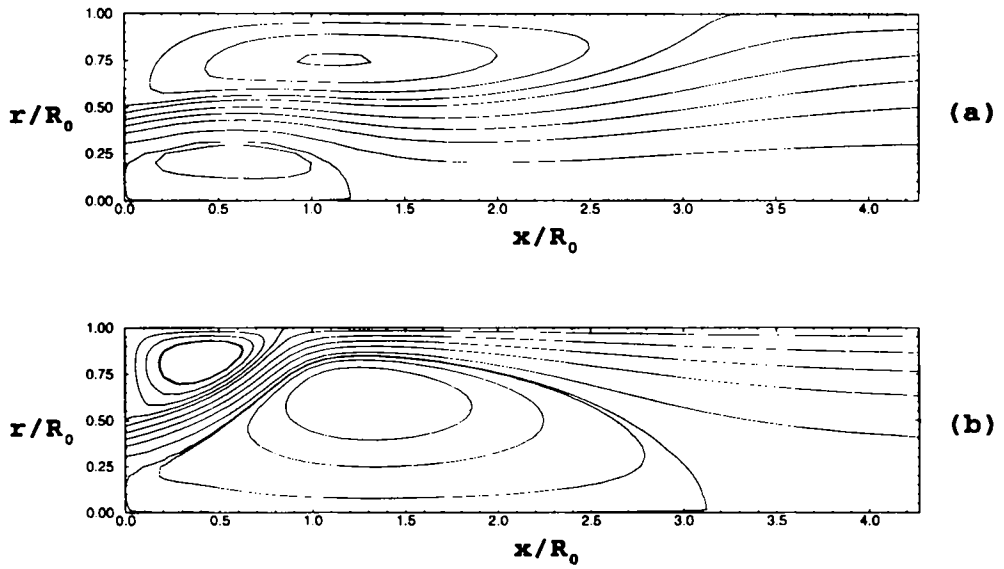

Figure 7. Flow patterns predicted by both the (a) lower and (b) upper branches at a swirl number of 0·21 using the k–ε model in conjunction with the second-order upwind scheme

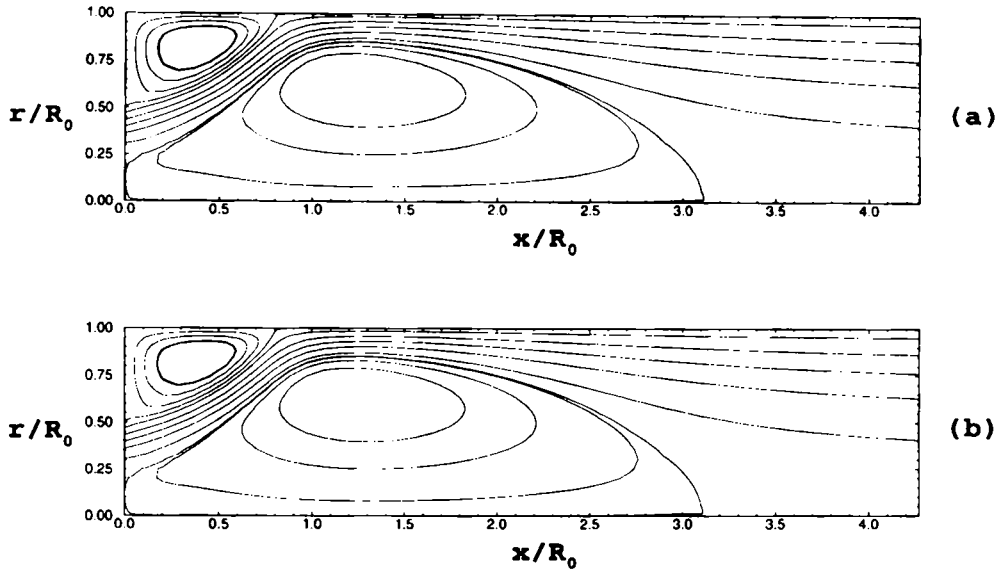

Figure 8. Flow patterns predicted by both the (a) lower and (b) upper branches at a swirl number of 0·25 using the k–ε model in conjunction with the second-order upwind scheme

low- and high-swirl flow patterns predicted by the lower- and upper-branch solutions respectively, while single high-swirl flow patterns are predicted by both the lower- and upper-solutions at a swirl number of 0·25 (Figures 8(a) and 8(b)). In other words, the flow changes from the low-swirl pattern to the high-swirl one as the swirl number increases from 0·21 to 0·25 along the lower branch. However, the high-swirl pattern is maintained as the swirl number decreases from 0·25 down to 0·21 following the upper branch. This result further confirms the postulation that the bifurcation of a confined swirling flow stems from a hysteresis effect as the high-swirl flow pattern changes to the low-swirl one by a gradual decrease in the swirl level.

It is noted that the predicted swirl level (SN = 0·25) by the second-order upwind scheme for the occurrence of the bifurcation is well below that predicted by the power law scheme (SN = 0·46). This is due to the fact that the latter underpredicts the IRZ stength owing to the severe numerical diffusion resulting from the low-order numerical scheme. Thus for the particular 38° swirl vane angle case (SN = 0·42) a single solution is predicted by the second-order upwind scheme, in contrast with the dual solutions predicted using the power law scheme. A comparison of the predicted axial velocity profiles shown in Figures 5 and 9 further reveals that the second-order scheme yields a result in much better agreement with the experimental data, since it gives a better prediction of the forward flow diverting outwards and around the IRZ. Therefore the bifurcation solution predicted by the power law scheme for this particular 38° swirl vane angle case is in fact numerical rather than physical, resulting from an underprediction of the IRZ strength owing to the use of a low-order scheme.

Effects of turbulence models

As reported by Weber *et al.*,[10] the turbulence models have a strong influence on the swirling flow predictions and the ASM is superior to the k–ε model. However, with the bifurcation of a confined swirling flow being discovered and the cause of the reported[1] poor performance of the

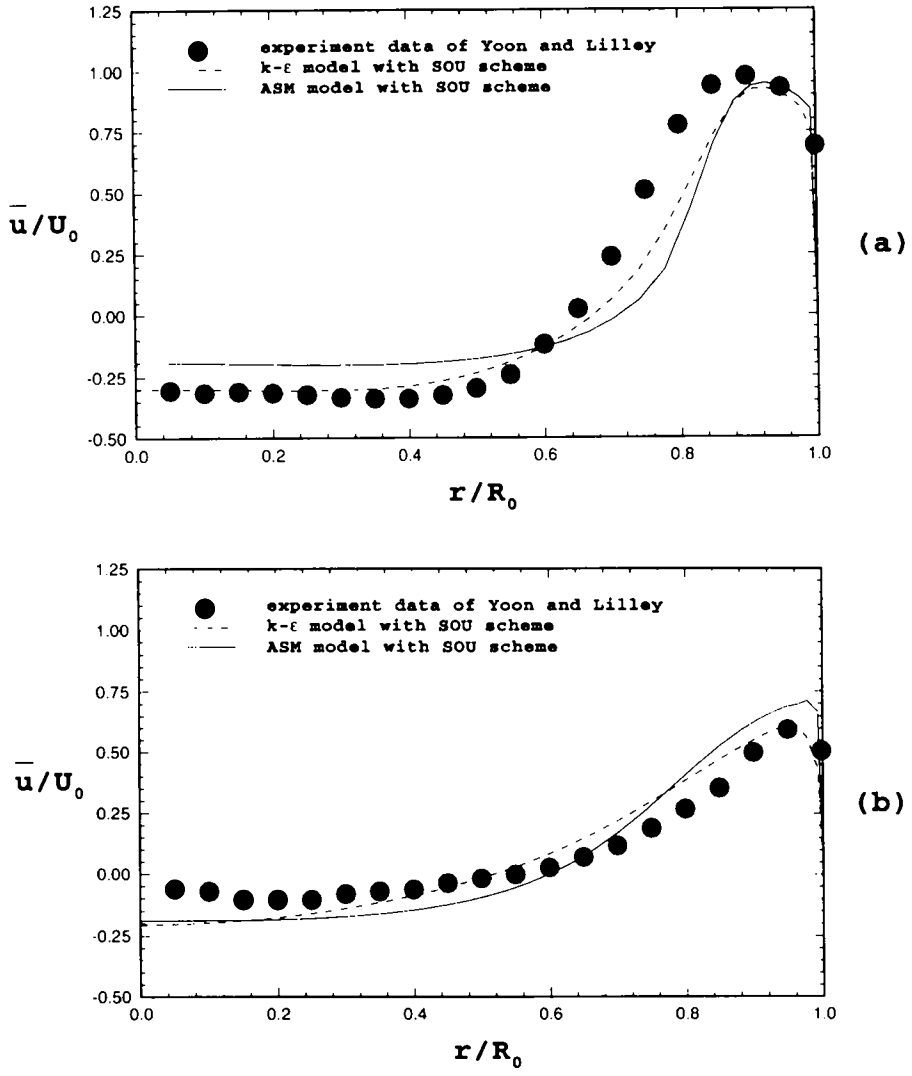

Figure 9. Axial velocity profiles for the 38° swirl vane angle case predicted by both the k–ε model and the ASM in conjunction with the second-order upwind scheme at x/R_0 = (a) 1·0 and (b) 2·0

k–ε model being identified, it is necessary to ascertain whether the effects of the turbulence models on the swirling flow predictions are as significant as reported, especially when the bifurcation is involved. To this end, the ASM in conjunction with the second-order upwind scheme is employed in computations for the present test case and the predicted ratio of the maximum reverse flow rate of the IRZ to that of the ERZ versus the swirl number is presented in Figure 10. In this case dual solutions are exhibited for swirl numbers smaller than 0·17, indicating that the bifurcation occurs independently of the turbulence models used. However, the bifurcation is predicted to occur at a swirl number slightly smaller than that predicted by the k–ε model if the same second-order upwind scheme is employed. Again two flow patterns (see Figures 11(a) and 11(b)) are predicted by the ASM at a swirl number of 0·13: the low-swirl one is predicted

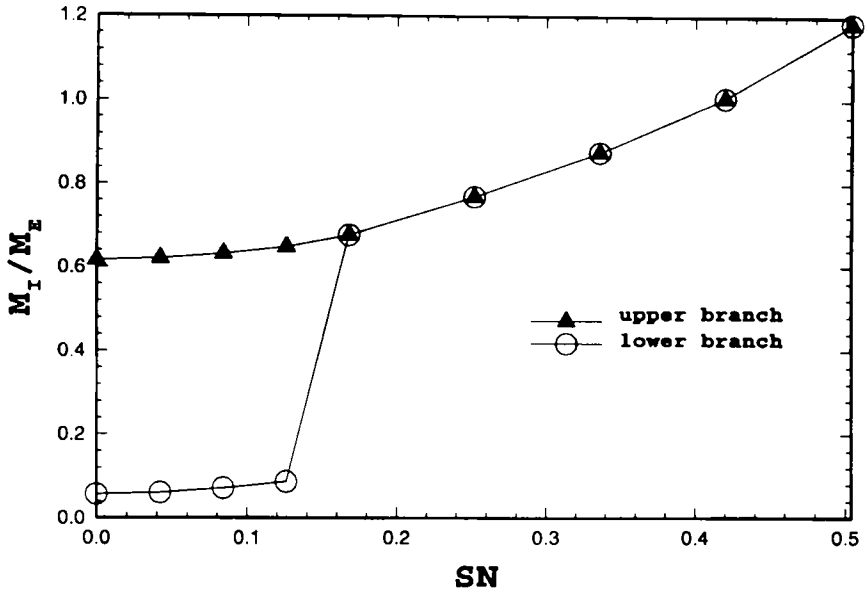

Figure 10. Ratio of the maximum flow of the IRZ to that of the ERZ versus the swirl number predicted by both the lower and upper branches using the ASM in conjunction with the second-order upwind scheme

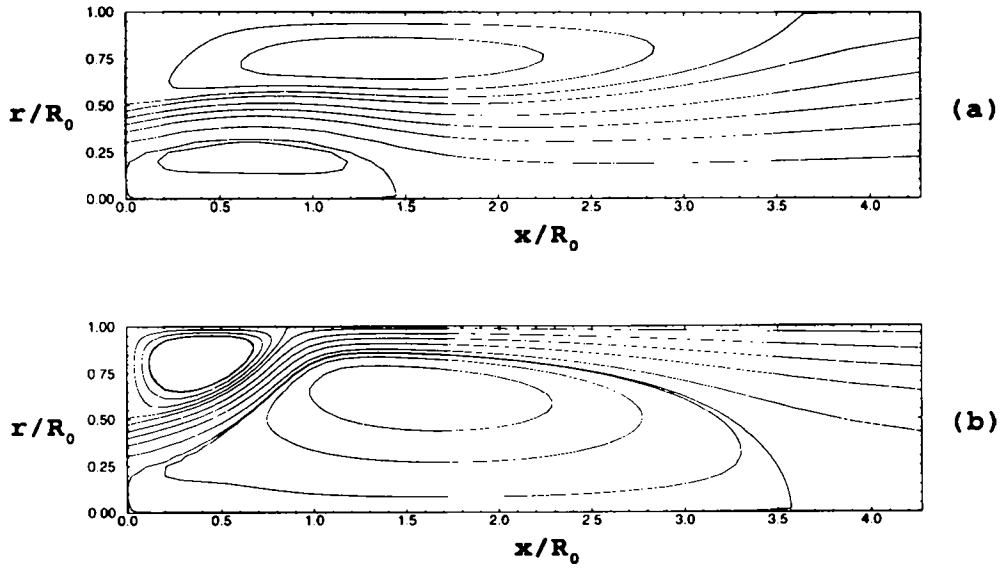

Figure 11. Flow patterns predicted by both the (a) lower and (b) upper branches at a swirl number of 0·13 using the ASM in conjunction with the second-order upwind scheme

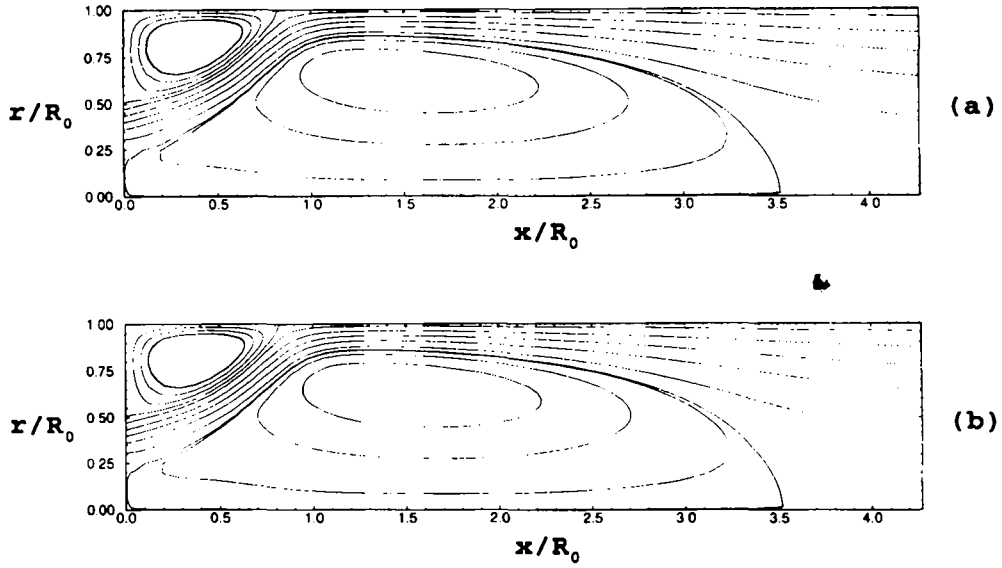

Figure 12. Flow patterns predicted by both the (a) lower and (b) upper branches at a swirl number of 0·17 using the ASM in conjunction with the second-order upwind scheme

by the lower branch and the high-swirl one by the upper branch. Both branch solutions, however, give identical high-swirl flow patterns for swirl numbers greater than 0·17 (Figures 12(a) and 12(b)). These results are qualitatively similar to those predicted by the k–ε model in conjunction with the second-order upwind scheme (Figures 7 and 8). The occurrence of the bifurcation may result in a situation which may mislead the evaluation of the turbulence models on the predictions of a confined swirling flow. For instance, if the upper-branch solution is picked up by the ASM and the lower-branch one by the k–ε model, or vice versa, a false conclusion may be reached that the ASM and the k–ε model perform very differently or the k–ε model performs poorly if the experimental result happens to coincide with the ASM result. Therefore knowing whether the bifurcation occurs is essential in evaluating the predictive capabilities of the turbulence models.

For the particular 38° swirl vane angle case it is interesting to note that by employing either the ASM or the k–ε model, a single high-swirl flow solution is yielded if the second-order upwind scheme is used in computations. The axial velocity profiles predicted by both the ASM and the k–ε model in conjunction with the same second-order upwind scheme exhibit a similar result which is in good agreement with the experimental data. A further examination of the predictions reveals that the ASM yields a better prediction in the near-wall region but a worse result in the central region. Both predictions are, however, in much better agreement with the experimental result in comparison with that predicted by the k–ε model in conjunction with the power law scheme (see Figures 5 and 9). Therefore the effects of the turbulence models on the swirling flow predictions are not as significant as those of the different-order numerical schemes, at least for the present flows with low swirl numbers. In other words, the k–ε model may produce sufficiently good predictions for confined swirling flows, a result in agreement with the work of Durst and Wennerberg.[11]

CONCLUSIONS

The bifurcation of a confined swirling flow was predicted numerically, with the effects of numerical schemes and turbulence models being investigated. The following conclusions were drawn from the present study:

1. Dual flow patterns at certain swirl numbers were obtained depending upon the branch solution examined. As the swirl number increases along the lower branch of the bifurcation, the flow pattern changes from a low-swirl one to a high-swirl one. As the swirl number decreases following the upper branch of the bifurcation, the flow can maintain itself in the high-swirl flow structure at the swirl numbers where it exhibits the low-swirl one in the lower branch, resulting from a hysteresis effect. The occurrence of the bifurcation of a confined swirling flow was predicted by both the k–ε model and the ASM, although the predicted swirl number range for the occurrence of the bifurcation varies.
2. For confined swirling flows the k–ε model results in predictions in good agreement with the experimental result and comparable with those yielded by the ASM, provided that high-order numerical schemes are used. This result is in agreement with the work of Durst and Wennerberg,[11] where satisfactory predictions by the k–ε model in conjunction with high-order convection–diffusion schemes were reported. The reported[1] poor performance of the k–ε model was clarified to be attributable to either the use of a low-order numerical scheme or the occurrence of dual flow patterns of the bifurcation.
3. As the first discovery of the bifurcation of a confined swirling flow, the present study was confined to numerical predictions on an isothermal flow field. Experimental verifications are required to ascertain such a bifurcation phenomenon. Furthermore, since combustion alters both the IRZ and ERZ strengths, the bifurcation of a confined swirling, reacting flow exhibits very different features from those of a non-reacting flow. This problem, which is of particular interest for swirl combustion, will be presented in a subsequent paper.

APPENDIX: NOMENCLATURE

$C_{\mathrm{ASM},1}$	constant
$C_{\mathrm{ASM},2}$	constant
C_k	constant
$C_{\varepsilon 1}$	constant
$C_{\varepsilon 2}$	constant
$C_{\varepsilon 3}$	constant
C_μ	constant
g	turbulent kinetic energy 'generation' ($g = \rho P$)
k	kinetic energy of turbulence
l	characteristic dimensional of flow passage
M	maximum reverse flow rate
p	pressure
P	turbulent kinetic energy 'production'
r	radial co-ordinate
R_o	chamber radius
R_i	inlet tube radius

R_h swirler hub radius
R_k constant
SN swirl number
u axial velocity
U_0 inlet average velocity
v radial velocity
w tangential velocity
x axial co-ordinate

Greek letters

ε turbulent dissipation rate
μ viscosity
μ^e effective viscosity ($\mu^e = \mu + \mu^t$)
μ^t turbulent viscosity
ρ density
σ Schmidt or Prandtl number

Subscripts

k turbulent kinetic energy
ε dissipation rate
in inlet
E external recirculation zone (ERZ)
I internal recirculation zone (IRZ)

Superscripts

$\overline{(\ )}$ Reynods-averaged value
$(\ )'$ fluctuational value

REFERENCES

1. D. G. Sloan, P. J. Smith and L. D. Smoot, 'Modeling of swirl in turbulent flow systems', *Prog. Energy Combust. Sci.*, **12**, 163–250 (1986).
2. F. Durst, A. Melling and J. H. Whitelaw, 'Low Reynolds number flow over a plane symmetric sudden expansion', *J. Fluid Mech.*, **64**, 111–128 (1974).
3. W. Cherdron, F. Durst and J. H. Whitelaw, 'Asymmetric flows and instabilities in symmetric ducts with sudden expansions', *J. Fluid Mech.*, **84**, 13–31 (1978).
4. I. J. Sobey, 'Observation of waves during oscillatory channel flow', *J. Fluid Mech.*, **151**, 395–406 (1985).
5. R. M. Fearn, T. Mullin and K. A. Cliffe, 'Nonlinear flow phenomena in a sudden symmetric expansion', *J. Fluid Mech.*, **211**, 595–608 (1990).
6. F. Durst, J. C. F. Pereira and C. Tropea, 'The plane symmetric sudden-expansion flow at low Reynolds numbers', *J. Fluid Mech.*, **248**, 567–581 (1993).
7. A. Restivo and J. H. Whitelaw, 'Turbulence characteristics of the flow downstream of a symmetric, plane sudden expansion', *Trans. ASME I: J. Fluids Eng.*, **100**, 308–310 (1978).
8. H. K. Yoon and D. G. Lilley, 'Five-hole pitot probe time-mean velocity measurements in confined swirling flows', *AIAA Paper 83-0315*, 1983.
9. H. K. Yoon and D. G. Lilley, 'Further time-mean measurements in confined swirling flows', *AIAA J.*, **22**, 514–515 (1984).
10. R. Weber, B. M. Visser and F. Boysan, 'Assessment of turbulence modeling for engineering prediction of swirling vortices in the near burner zone', *Int. J. Heat Fluid Flow*, **11**, 225–235 (1990).
11. F. Durst and D. Wennerberg, 'Numerical aspects of calculation of confined swirling flows with internal recirculation', *Int. j. numer. methods fluids*, **12**, 203–224 (1991).

12. G. J. Sturgess, S. A. Syed and K. R. McManus, 'Importance of inlet boundary conditions for numerical simulation of combustor flows', *AIAA Paper 83-1263*, 1983.
13. B. E. Launder and D. B. Spalding, 'The numerical computation of turbulent flows', *Comput. Methods Appl. Mech. Eng.*, **3**, 269–289 (1974).
14. S. V. Patankar, *Numerical Heat Transfer and Fluid Flow*, Hemisphere, Washington, DC, 1980.
15. S. V. Patankar, 'A calculation procedure for two dimensional elliptic situations', *Numer. Heat Transfer*, **4**, 409–425 (1981).
16. M. C. Melaaen, 'Calculation of fluid flows with staggered and nonstaggered curvilinear nonorthogonal grids—the theory', *Numer. Heat Transfer B*, **21**, 1–19 (1992).